


Three-dimensional multiscale flow structures behind a wall-mounted short cylinder based on tomographic particle image velocimetry and three-dimensional orthogonal wavelet transform

Hiroka Rinoshika¹, Akira Rinoshika¹ and Jin-Jun Wang²

¹*Department of Mechanical Systems Engineering, Graduate School of Science and Engineering, Yamagata University, 4-3-16 Jonan, Yonezawa-shi, Yamagata 992-8510, Japan*

²*School of Aeronautic Science and Engineering, Beijing University of Aeronautics and Astronautics, 37 Xueyuan, Haidian District, Beijing 100191, China*

 (Received 4 November 2019; accepted 28 July 2020; published 2 September 2020; corrected 4 April 2023)

Three-dimensional (3D) flow structures around a wall-mounted short cylinder of height-to-diameter ratio 1 were instantaneously measured by a high-resolution tomographic particle image velocimetry (Tomo-PIV) at Reynolds number of 10 720 in a water tunnel. 3D velocity fields, 3D vorticity, the Q criterion, the rear separation region, and the characteristic of arch type vortex and tip vortices were first discussed. We found a strong 3D W-type arch vortex behind the short cylinder, which was originated by the interaction between upwash and downwash flows. This W-type arch vortex was reshaped to the M-shaped arch vortex downstream. It indicated that the head shape of the arch vortex structure depended on the aspect ratio of the cylinder. The large-scale streamwise vortices were originated by the downwash and upwash flows near the center location of W-type arch vortex. Then the 3D orthogonal wavelet multiresolution technique was developed to analyze instantaneous 3D velocity fields of Tomo-PIV in order to clarify 3D multiscale wake flow structures. The W-type shape arch vortex was extracted in the time-averaged intermediate-scale structure, while an M-shaped arch vortex was identified in the time-averaged large-scale structure. The tip vortices distributed in the time-averaged large- and intermediate-scale structures. The instantaneous intermediate-scale upwash vortices played an essential role in producing W-type head of arch structure. It was also observed that strong small-scale vortices appeared in the shear layer or near the bottom plate and most of them were contained in the intermediate-scale structures.

DOI: [10.1103/PhysRevE.102.033101](https://doi.org/10.1103/PhysRevE.102.033101)

I. INTRODUCTION

Strongly three-dimensional (3D) complex flow structures are originated by a finite circular cylinder, and the aspect ratio of the cylinder, i.e., the ratio of the height and diameter, has a significant effect on the wake structure. They are different from the structures generated by an infinite circular cylinder [1,2], owing to the effect of the cylinder free end and the connection between cylinder and ground plane [3–6]. Many important engineering applications meet this geometry, such as reducing drag and noise induced by the design of heat exchangers, structural vibrations, automobile, offshore structures, and so on. The investigation of the complex flow structures generated by finite circular cylinder is found in the literature. The Kármán vortex shedding from both sides of the cylinder, the horseshoe vortex and base vortex near the ground plane [3,7], and a pair of streamwise counter-rotating tip vortices generating from the free end [8–10] can be observed. Lee [11] also informed that the structures of Kármán vortex cell are reduced when the aspect ratio decreases. The tip vortices [12–14] and a horseshoe vortex [15,16] exist around a low-aspect-ratio cylinder, while alternating vortex shedding, i.e., Kármán vortex street, cannot be found. In the case of a lower aspect ratio, an “arch-type vortex” structure appears behind the cylinder [11] since the vortex from the free-end surface is influenced by the vortices shedding from the sides before reattaching to the ground. Sumner [17] and Porteous

et al. [18] report about the wake structures of a finite-height cylinder. Recently, Rinoshika and co-workers [19–22] used the two-dimensional particle image velocimetry (PIV) measurement to clarify the wake structures, and proposed inclined holes and a horizontal hole to control the flow around the low-aspect-ratio cylinder. Until now, most of the researches on the 3D wake structures behind a finite-height cylinder have been performed based on the two-dimensional PIV measurement. Based on the two-dimensional PIV measurement, Pattenden *et al.* [4] analyzed the mean flow fields behind a finite cylinder with an aspect ratio 1 and gave a topological structure of Fig. 1(a). Besides a horseshoe vortex and tip vortices, a large-scale stump arch vortex behind the cylinder is observed. Recently, Zhu *et al.* [23] first applied Tomographic PIV of six cameras (2058×2456 pixels²) to measure the 3D flow structures around a short wall-mounted cylinder (diameter = 20 mm) having an aspect ratio of 2. They first found that the arch vortex behind the cylinder exhibits a 3D M shape [Fig. 1(b)]. This indicates that the shape of the arch vortex may depend on the aspect ratio of a short cylinder, which is a very interesting and challenging problem. Therefore, it becomes a target of this study. On the other hand, the 3D multiscale flow structure analysis tool is essential to reveal the 3D flow structures around a short wall-mounted cylinder even though Zhu *et al.* [23] applied POD to analyze tomographic PIV data in the energy distribution.

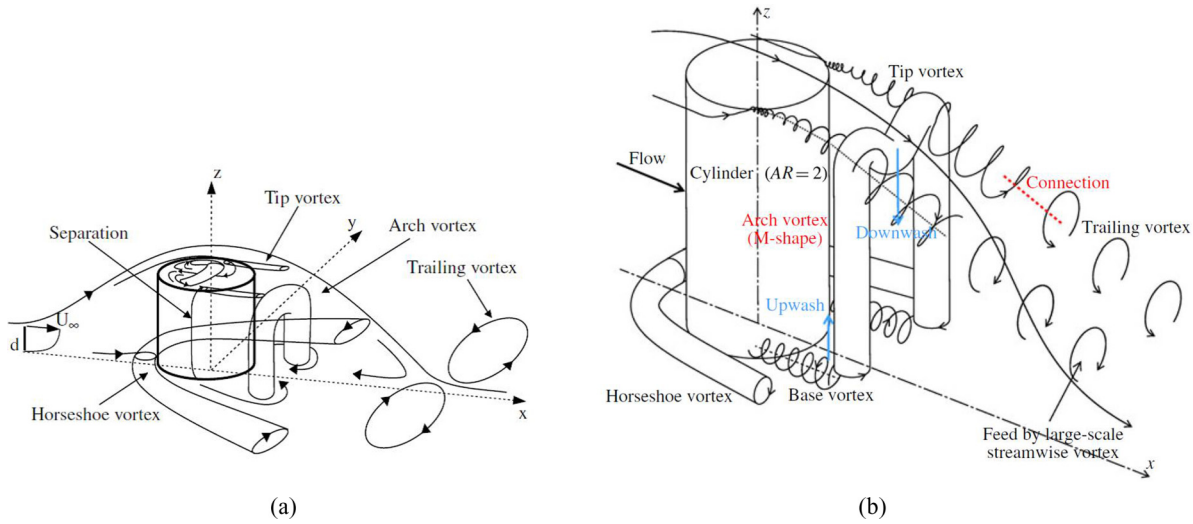


FIG. 1. Sketch of the time-averaged flow field over a short circular cylinder. (a) Aspect ratio $L/D = 1$ [4]. (b) Aspect ratio $L/D = 2$ [23].

After Meneveau [24] and Yamada and Ohkitani [25] resolved the one-dimensional experimental turbulence data into several scales by using the statistical method, the orthogonal wavelet transform, as an important multiscale tool, was widely used on analyzing various turbulent flow structures. Several review reports on wavelet transform applications in the area of fluid mechanics have been introduced by Farge [26,27], Schneider and Vasilyev [28], and Rinoshika [29]. A one-dimensional orthogonal wavelet multiresolution technique was developed to extract the various scale turbulent structures including large-scale structures, secondary spanwise structures, and so on in the near wake of a circular cylinder by Rinoshika and Zhou [1]. Based on the same technique, they further studied the effect of various wake-generating bodies or Reynolds number on the different scale turbulent structures in the near and far wakes [2,30–32]. Furthermore, this wavelet technique was also applied to decompose the three-component vorticity data of cylinder wakes into several wavelet components according to their central frequencies [33–35]. As for industrial applications, the orthogonal wavelet transform was used to reveal the wake structures around vehicle door mirror based on LES simulations [36] and PIV measurement data [37,38]. This wavelet technique is also employed to reveal the various scale flow structures in the barchan dune wakes [39,40]. Farge *et al.* [41] developed a coherent vortex simulation method decomposing the turbulent structures into coherent and incoherent structures based on 3D orthogonal wavelets. Recently Stefano [42] also applied wavelet multiresolution analysis to identify and track energy-containing motions of bluff-body flows for constructing a high-fidelity physics-based adaptive LES method. The application of a three-dimensional orthogonal wavelet transform on three-dimensional experimental turbulence data motivates the present investigation.

In order to clarify the 3D wake flow structures of low-aspect-ratio cylinder, the three-dimensional velocity fields behind a short circular cylinder of a diameter $D = 70$ mm (aspect ratio 1) were first measured by tomographic particle image velocimetry (Tomo-PIV) of high-resolution cameras in a water tunnel. The measured 3D velocity distribution,

the vorticity, the Q criterion, the rear separation region, and the characteristic of arch type vortex and tip vortices were analyzed. Then, a 3D orthogonal wavelet multiresolution technique was developed to analyze the 3D various scale flow structures based on Tomo-PIV data.

II. EXPERIMENTAL APPARATUS AND TOMOGRAPHIC PIV SETUP

Our experiment was performed in a circular open water tunnel. The test section has a size of 3000 mm(length) \times 600 mm(width) \times 700 mm(height). As shown in Fig. 2, a short circular cylinder with a height of $H = 70$ mm and a diameter of $D = 70$ mm (aspect ratio $H/D = 1$) was placed on the central axis of the bottom wall 1200 mm downstream of the test section entrance. The blockage ratio of model in this experiment is $\Psi = S_m/S_t = 0.012$. Here the S_m is the streamwise sectional area of model, and the S_t is that of useful test section. The streamwise, spanwise, and longitudinal directions were respectively indicated by the x , y , and z axes. The center of the cylinder bottom surface is defined as the origin

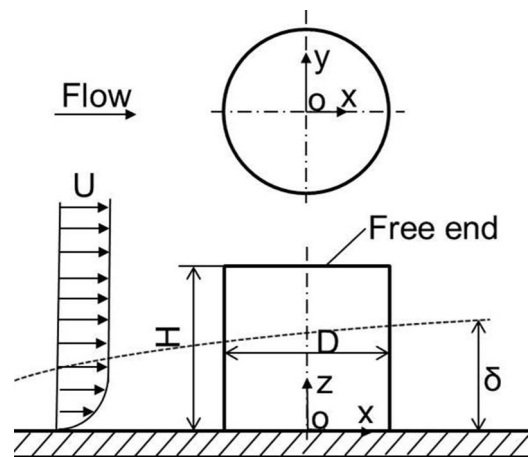


FIG. 2. Experimental setup and a surface-mounted finite length cylinder model.

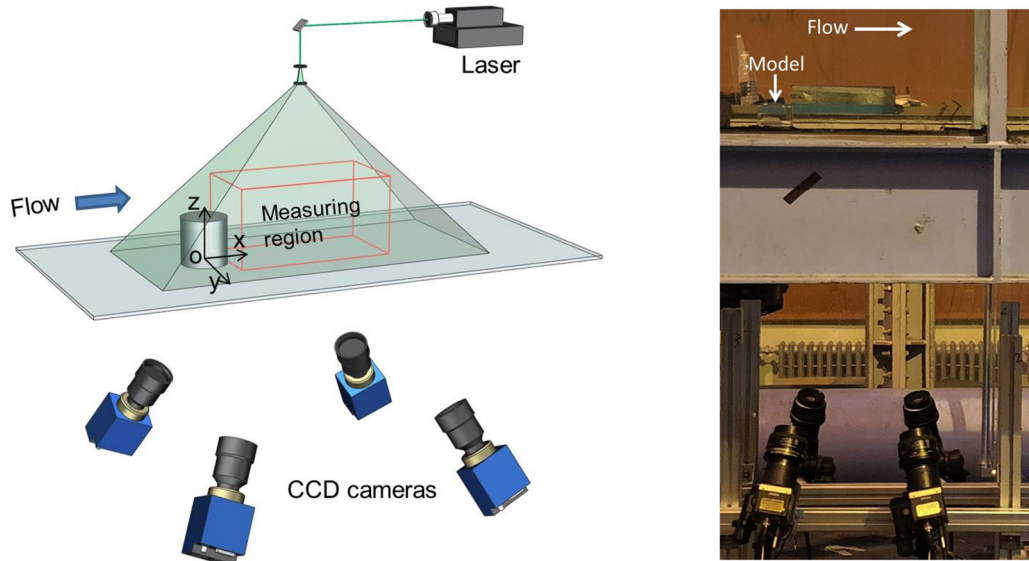


FIG. 3. Tomographic PIV setup.

of the coordinate system. A free stream velocity was fixed at $U = 0.162$ m/s, corresponding to Reynolds number $Re(\equiv UD/\nu)$ of 10 720. The experimental apparatus for Tomo-PIV measurements is shown in Fig. 3. The PIV tracer particles of a mean diameter $10\ \mu\text{m}$ were adopted. The response time of the particles based on the free-stream velocity was $1.6\text{--}2.8 \times 10^{-5}$ s. Illumination was provided by a dual-head Nd:YAG laser (500 mJ/pulse, 532 nm wavelength) with a pulse separation time of 3 ms, which yielded average displacements of approximately 0.48 mm (8 pixels) in the free-stream region. The optical lenses and the mirror were designed to generate an 80-mm-thick light sheet illuminating the tracer particles around the cylinder. The light sheet was perpendicular to the test section bottom. Four high-resolution (6600×4400 pixels², 12 bit) double-exposure charge-coupled device cameras (IMPERX SM-CCDB29M2) were applied to record the measurement domain simultaneously. The viewing angle was approximately 47° between cameras. The laser and cameras were controlled by a synchronizer and the sampling frequency was set at $f_s = 0.25$ Hz.

The measurement volume was in the coordinate range [[34], 270], [−70; 70], [0; 100] (mm) with a digital imaging resolution of 0.075 mm per pixel, so that its corresponding physical domain had a size of $245 \times 140 \times 100$ mm³ ($3.5D \times 2D \times 1.43D$). Tomo PIV was applied in the present investigation for its ability to display the distribution of average and instantaneous three-dimensional velocity. The 3D vector calculation was performed through a multipass correlation analysis with a deforming interrogation window. In the final pass, the interrogation volume was $32 \times 32 \times 32$ voxel with 50% overlap, resulting in to a spatial resolution of 2.4 mm and a vector pitch of 2.4 mm. The uncertainty in the mean flow fields could be evaluated by $\varepsilon_u = \sigma_u / \sqrt{N_s}$ [23] and $\varepsilon_u = 0.0045$. Here $\sigma_u = u'/U$ is the normalized standard deviation and N_s is the number of uncorrelated samples. In order to extract the 3D flow structures more clearly, a Gaussian smoothing [23,43] was used to remove residual noise

and small structures in the nondimensional vorticity and other volumetric data fields in the present study.

In order to estimate the boundary layer characteristics on the ground plane, the profiles of mean streamwise velocity and turbulence intensity were measured by laser doppler velocimeter. The profiles of mean streamwise velocity and turbulence intensity, normalized by free stream velocity U , at the center location of the cylinder in the flat-plate boundary layer are shown in Fig. 4. All data were obtained with no cylinder. At the location of the cylinder, the boundary layer thickness δ is 24.6 mm, which provided a thickness-to-diameter ratio of $\delta/D = 0.35$ in this study.

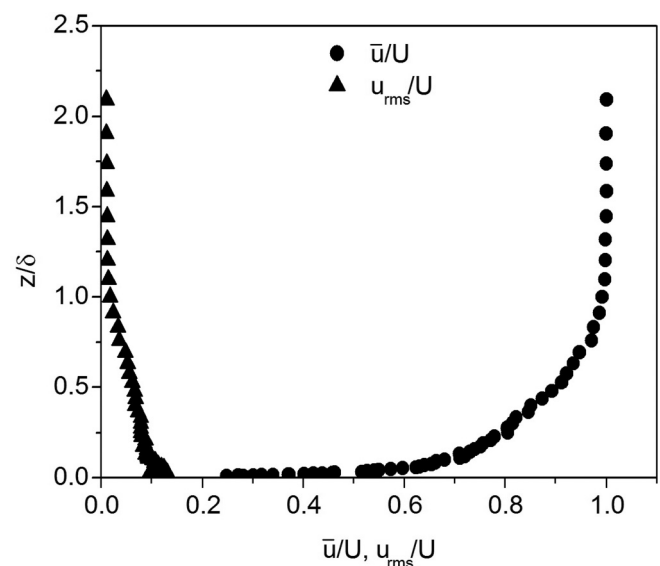


FIG. 4. Profiles of mean streamwise velocity and turbulence intensity (no cylinder) at the center location of the cylinder in the flat-plate boundary layer.

An important effect of the boundary layer thickness on the wake flow characteristics of a finite-length cylinder was observed at $\delta/D \approx 1.02$ [44], in which a significant upwash flow was induced by the base vortex and the thickness of the boundary layer may make the stronger upwash flow. In this study it may be considered as a weak effect of the boundary layer thickness ($\delta/D = 0.35$) on the wake flow of a short cylinder. Hearst *et al.* [45] investigated the effect of turbulence intensity on the wake of a turbulent boundary layer immersed cube, and found that the wake flow characteristics of a short cylinder are independent of turbulence intensity.

In our previous paper [19], the frequency characteristics on the wake flow structure of low-aspect-ratio cylinder has been analyzed based on two-dimensional PIV. To consider the effects of Reynolds number on the wake of the short cylinder, two-dimensional PIV measurements were carried out in the range of $Re = 7100$ to 13550 . We found that the velocity profile is (not shown here) independent of Reynolds number the short cylinder wake of aspect ratio 1, implying few effects of Reynolds number on the wake structures. Therefore, Tomo-PIV measurements of 3D wake flow fields were performed at $Re = 10720$ in this study.

III. TIME-AVERAGED 3D WAKE STRUCTURES

Figure 5 shows the 3D isosurface of $u/U = 0$ and the time-mean contour of the streamwise velocity behind the short cylinder. The isosurface of $u/U = 0$, which is averaged over 400 snapshots (the convective time $[(\frac{400}{f})(\frac{U}{D})]$ is 3703), exhibits the 3D rear recirculation zone. Near the plane of $y/D = 0$, a lower surface is clearly identified, which corresponds to the one found by Zhu *et al.* [23]. Such concavity region is formed due to the strong downwash flow from the free end surface. The recirculation zone gradually contracts along the main flow direction, and comes to an end at the downstream location of about $x/D = 1.6$ owing to the interaction of the vortex shedding from the cylinder side wall and free end.

Figure 6 shows the 3D mean streamlines of rear recirculation zone near the short cylinder. A 3D large-scale vortex resulting from the strong downwash flow is evidently observed, and the center line of the large-scale vortex is bent in the form

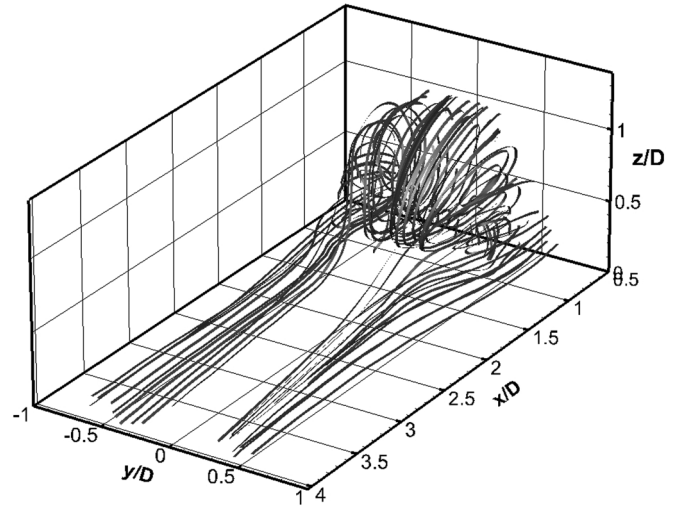


FIG. 6. The 3D mean streamlines.

of a half circle. The vortex diameter at the center plane of $y/D = 0$ is the largest and shrinks close to the ground plane due to the interaction between the vortex shedding from the cylinder side wall and ground plane.

It is well known that the tip vortex pair originating from the edge of free end is important in the wake of the finite-length cylinder. Figure 7 displays the 3D isosurface of mean streamwise x vorticity of $\bar{\omega}_x D/U = \pm 0.45$ behind the short cylinder. It is plotted as red and green indicating positive and negative vortex, respectively. A streamwise vortex pair occurring from the free end surface is evidently extracted from Tomo-PIV. The streamwise vortex pair exhibits a dipole type and extends downstream to the ground plane due to the effect of the downwash flow. At the location of $x/D = 1$, a pair of base vortices is also observed.

It is a well-known fact that the arch vortex exists in the low-aspect-ratio cylinder wake [4]. Zhu *et al.* [23] had

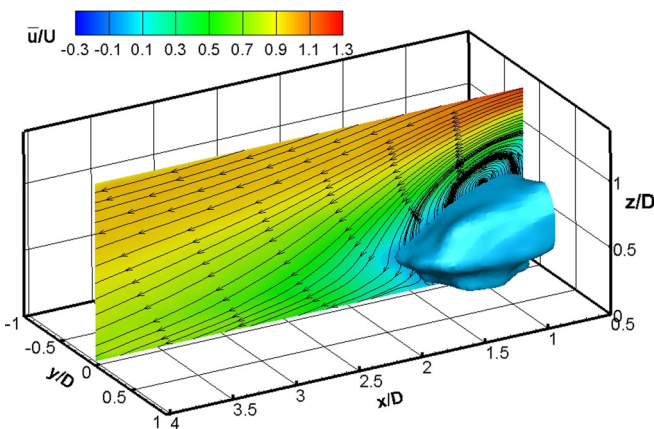


FIG. 5. The mean isosurface of $\bar{u}/U = 0$ with the streamlines and contour of the streamwise velocity.

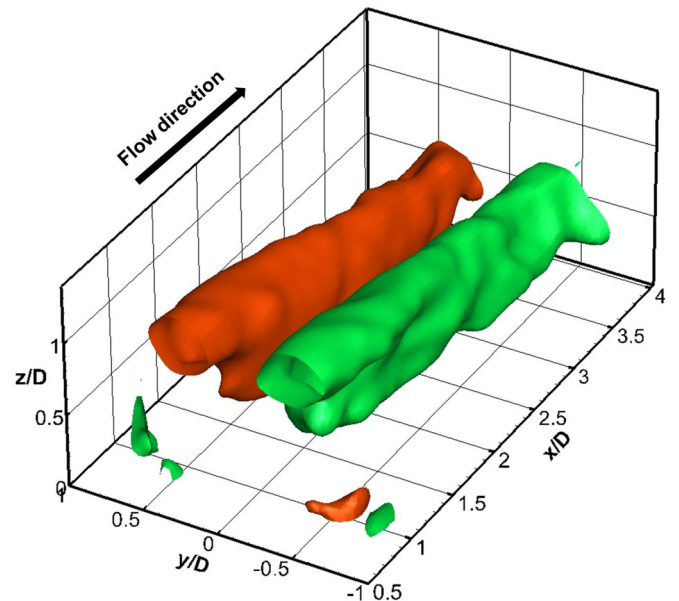


FIG. 7. The isosurface of streamwise vorticity $\bar{\omega}_x D/U = \pm 0.45$.

experimentally confirmed the existence of the 3D arch vortex in the cylinder wake with an aspect ratio of 2 by Tomo-PIV. In this study, we use the Q criterion to extract the arch vortex structure and its main features in the cylinder wake with an aspect ratio of 1.

The Q criterion [36] is calculated by

$$Q = (\|\Omega\|^2 - \|S\|^2)/2, \tag{1}$$

where Ω and S represent the tensor of the angular velocity and the tensor of strain rate, respectively. The $\|\cdot\|$ is the Euclidean norm. The Q criterion may be used to identify the vortical structures by the excess rotation relative to the strain rate, which is normalized by $(U/D)^2$ in this study.

Figure 8(a) shows the 3D isosurface distribution of $Q/(U/D)^2 = 0.7$ colored by the streamwise vorticity $\bar{\omega}_x D/U$ in the time-averaged flow field. It is clearly observed that the 3D arch vortex behind the short cylinder exhibits an M shape [23] due to the downwash flow. However, on increasing $Q/(U/D)^2$ to 7, indicated by Fig. 8(b), a W-type head shape stands on the ground plane behind the short cylinder, instead of a reversed U shape [4] or an M shape [23], which represents the strong arch vortex structure. Two concave parts near the two sides of the horizontal part are evidently observed in the W-type arch structure, which is caused by the downward flow from the free end and tip vortex. The center convex of the horizontal part on the W-type arch structure is induced due to the strong upwash effect of the large flow separation behind the cylinder, as indicated in Fig. 6. Being different from the M shape [23], the larger distance between two tip vortices results in the weaker effect of tip vortices on the center part of the head even though they have strong vorticity at the two sides of the arch head, which is described later.

The time-averaged streamlines and the contour of the streamwise velocity in the (x, z) plane of $y/D = 0$ and 0.4 are described in Fig. 9. They visualize the distribution of 3D velocity field in two side view planes. The flow field discussed here is not a planar flow but has a highly three-dimensional feature. At $y/D = 0$, the separation region is spread over most of the cylinder height. The downwash flow originating from the free end surface doesn't reach the ground plane due to the effect of the upwash flow. The height and size of the large-scale vortex decrease and the separation region becomes smaller from plane $y/D = 0$ to 0.4 . Meanwhile, the height of the saddle point S , as indicated in Fig. 9, increases. The downwash flow that the interaction among the vortices causes may become weaker moving away from the center plane.

Figure 10 shows the time-averaged streamlines with the contour of the mean streamwise velocity in the (x, y) plane at $z/D = 0.2$ and 0.5 . It visualizes the distribution of 3D velocity field in the top view planes (Fig. 7). A pair of large counter-rotating vortices can be clearly seen in the two planes. At the height of $z/D = 0.5$, the distance between two vortices and the separation region is larger than that of other heights. The strong separation flow from the side walls may make the separation region become wider at $z/D = 0.5$ due to a weak effect of ground plane and free end. However, the vortices disappear above the position of $z/D = 0.8$ (not shown here).

The time-averaged velocity vectors with the contour of the streamwise vorticity $\bar{\omega}_x D/U$ in the (y, z) plane at $x/D = 0.7$

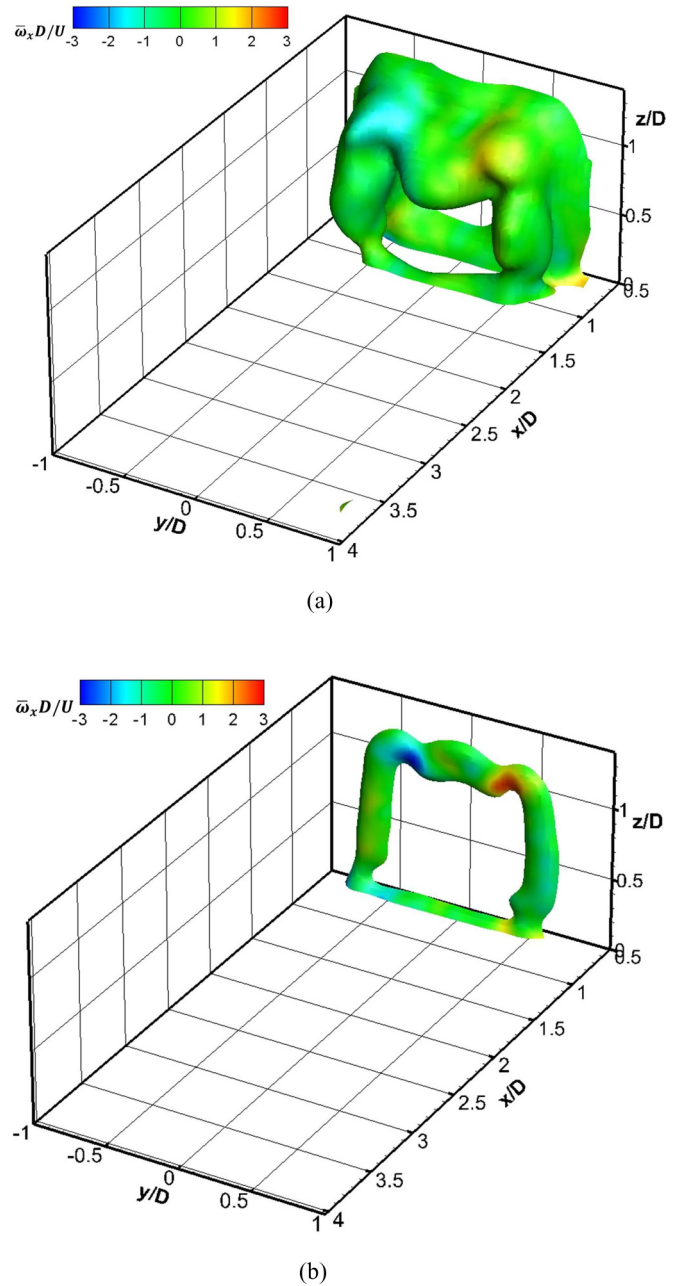


FIG. 8. The mean isosurface of $Q/(U/D)^2$ colored by the streamwise vorticity $\bar{\omega}_x D/U$. (a) $Q/(U/D)^2 = 0.7$. (b) $Q/(U/D)^2 = 7$.

and 1.0 are plotted in Fig. 11. They visualize the distribution of 3D velocity and vorticity fields in the rear-view planes (Fig. 7). At the location of $x/D = 0.7$, a pair of strong tip vortices generated by the free end is clearly observed. The upwash and downwash flows can be seen between two tip vortices near the top surface of the cylinder, which is an important reason of forming the W-type head of arch structure. At the downstream of $x/D = 1.0$, the strong downwash is found near the free end surface and two tip vortices are deformed. It is inferred that the W-type head of arch vortex is reshaped at this location and form an M-shaped arch vortex [Fig. 8(a)] [23]. Meanwhile, a vortex pair, generated from the interaction between the downwash flow and upwash flow,

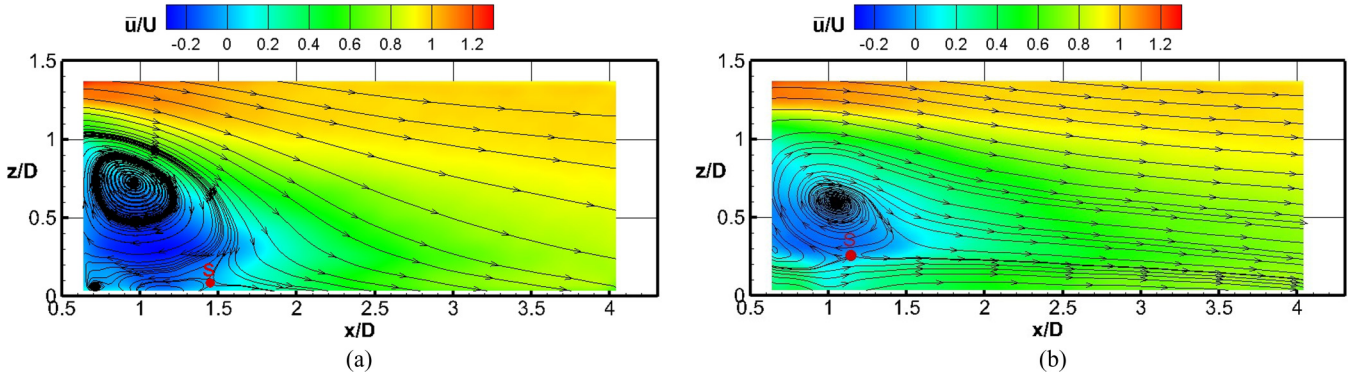


FIG. 9. The mean streamlines and the contour of the mean streamwise velocity \bar{u}/U in the (x, z) plane. (a) $y/D = 0$. (b) $y/D = 0.4$.

is observed at the height of $z/D = 0.5$, which originates the large-scale streamwise vortices (to be discussed in Sec. IV). At the downstream, two tip vortices become dispersed and move toward the ground due to the effects of the downwash flow and other vortices. Meanwhile, their vorticity intensity decreases evidently.

IV. INSTANTANEOUS 3D MULTISCALE WAKE STRUCTURES

Figure 12(a) shows a 3D distribution of the instantaneous Q criterion with isosurface of $Q/(U/D)^2 = 2.5$ colored by the streamwise vorticity $\omega_x D/U$. It is observed that 3D various scale vortical structures are clearly observed. An instantaneous W-type arch vortex, as indicated by 1 in Fig. 12(a), is very similar to that of the time-averaged flow field of Fig. 8. The free end originates the top flow separation and tip vortices at the trailing edge, which induces a W-shape arch vortex. The center convex of the horizontal part of the W-type arch structure is produced due to the upwash effect of the large flow separation behind the cylinder, as shown in Fig. 7 of the time-averaged flow field. The two concave parts of the horizontal part are caused by the downward flow and tip vortices. Therefore, the tip vortices and free end flow separation results in the “shoulders” and “head” of the arch

structure. It may be said that the arch vortex consists of two vertical shedding vortices (the side wall) and one horizontal shedding vortex (the free end), which is connected by two tip vortices. Therefore, the arch structure model of this study is different from Pattenden *et al.* [4] and Zhu *et al.* [23]. One of reasons that is different from Zhu *et al.* [23] is the aspect ratio of cylinder. For aspect ratio 1, the height of the free end becomes low or the distance of the two tip vortices originating from the free edge end becomes large, as shown in Fig. 11(a), which induces the strong upwash flows between two tip vortices and forms a W-shaped arch vortex. As for aspect ratio 2 of the cylinder (Zhu *et al.* [23]), the two tip vortices come close to each other or the height of free end becomes high, which weakens the upwash flow and forms a M-shaped arch vortex. It is implied that the head shape of the arch vortex structure depends on the aspect ratio of the cylinder.

It is also clearly observed that the W-type arch vortex rapidly breaks down into several fragments downstream. For example, the several vortex structures labeled 2 and 3 may be identified as fragments of the arch vortices as shown in Fig. 12(a). It may be inferred that strong downwash from the center of the surface end is produced as Re increases, which results in the arch vortex breaking down rapidly and a more evident W-shaped arch vortex. A large-scale stream-

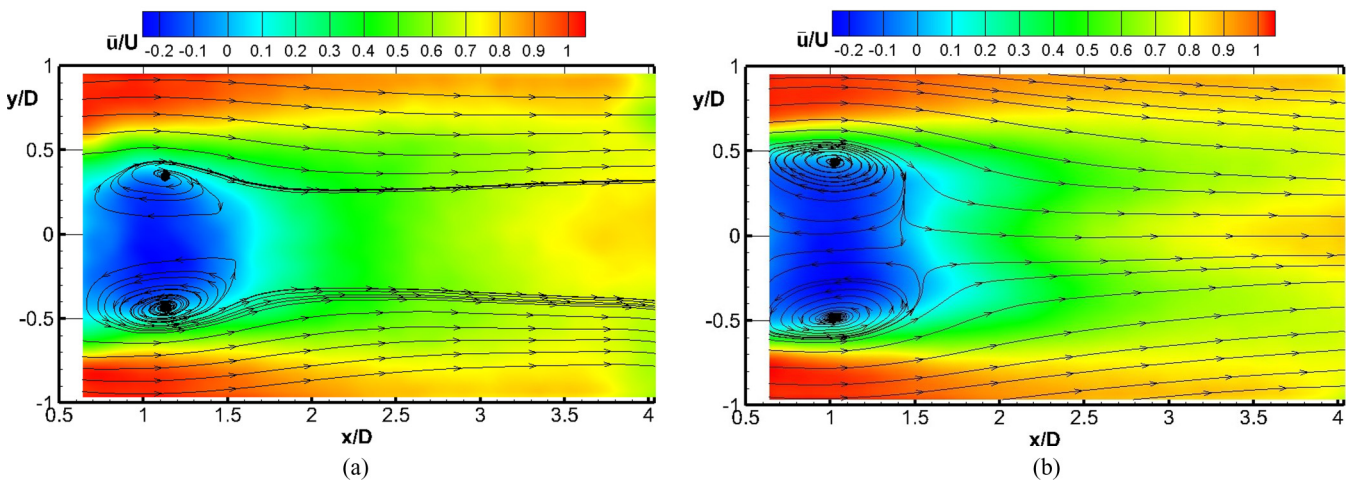


FIG. 10. The mean streamlines and the contour of the mean streamwise velocity \bar{u}/U in the (x, z) plane. (a) $z/D = 0.2$. (b) $z/D = 0.5$.

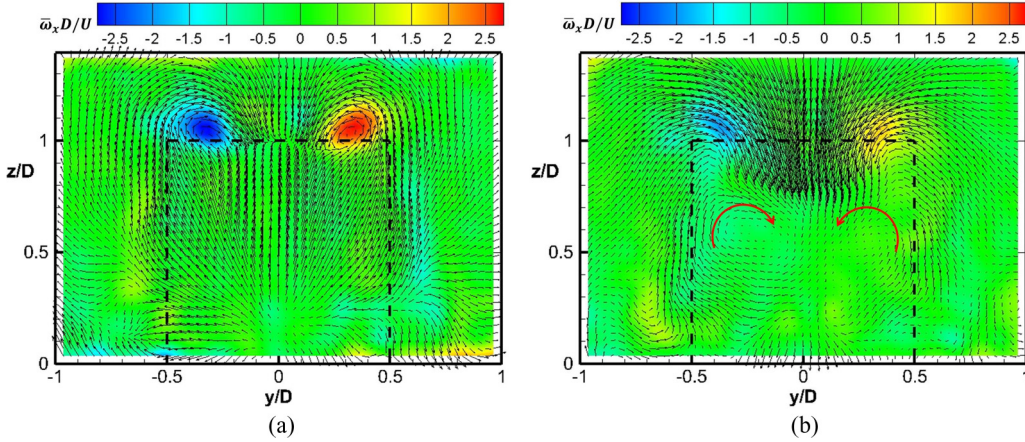


FIG. 11. The mean velocity vectors with the contour of the mean streamwise vorticity $\bar{\omega}_x D/U$ in the (y, z) plane. (a) $x/D = 0.7$. (b) $x/D = 1.0$.

wise vortex (indicated by 4), also found by Zhu *et al.* [23], can be evidently observed in the instantaneous flow field in Fig. 12(a) due to the downwash and upwash flows and interacting with the other vortical structures. Figure 12(b) shows another the instantaneous Q criterion distribution with isosurface of $Q/(U/D)^2 = 2.5$ colored by the streamwise vorticity $\omega_x D/U$, in which an instantaneous W-type arch vortex (indicated by I) is also extracted. Meanwhile two large-scale streamwise vortices, indicated by II and III in Fig. 12, are clearly observed. It is evident that these two vortices are originated by the downwash and upwash flows near the center location of the W-type arch vortex and are connected with fragments of the arch vortices or shedding vortices of the side wall. The large-scale streamwise vortices are also analyzed later.

Based on the above results, the mean vortical structures around the short cylinder of aspect ratio 1 are sketched in Fig. 13, which includes tip, horseshoe, base, arch, and trailing vortices and their locations. Although these vortices have been suggested in the literature, three-dimensional configurations of W-type arch vortex is first observed and proposed in this Tomo-PIV measurement. In particular, the interaction among vertical shedding vortices of the side wall, horizontal shedding vortex of the free end and tip vortices, which form a W-type arch vortex, could not be found in the planar PIV measurement of the previous experiments [19–22].

In order to reveal the 3D multiscale flow structures behind the short cylinder, the 3D wavelet multiresolution method, described in the Appendix, is first applied to 3D instantaneous velocity field [Fig. 12(a)] of Tomo-PIV in this paper. 3D velocity data are decomposed into three velocity wavelet components based on their characteristic scales or central scales, which are representative of the large-, intermediate-, and small-scale structures in this study, by using orthogonal wavelet multiresolution technique. Here the large- and intermediate-scale structures are respectively represented by wavelet component of levels 1 and 2, and the small-scale structure consists of level 3 and level 4. Based on the resolution of our Tomo-PIV, the large-scale structure has the central scale of $a/D = 0.55$, the intermediate-scale structure has the central scale of $a/D = 0.27$, and the small-scale structure has

the central scale of $a/D = 0.14$. Here a represents the wavelet central scale.

Figures 14(a)–14(d) exhibit the measured and three scales of the 3D instantaneous $Q_i/(U/D)^2$ isosurface with colored by the streamwise vorticity $\omega_{xi} D/U$. Here i represents the wavelet level. In the large-scale structures of level 1, as shown in Fig. 14(b), a large-scale arch vortex, corresponding to vortical structure labeled 2 in Fig. 14(a), is clearly observed. Meanwhile, two large-scale streamwise vortices with the positive and negative senses of rotation are also extracted, which match the measured instantaneous flow structures labeled 3 and 4 in Fig. 14(a). They go through the center of arch vortex and develop to the downstream, which also dominates the flow structures downstream.

As decreasing to intermediate-scale structures of level 2 in Fig. 14(c), several fragments of vortices labeled 1 are broken down downstream, and the intermediate-scale streamwise vortices and trailing vortices are extracted.

In the small-scale structure of level 3 (with the central scale of $a/D = 0.14$), as displayed in Fig. 14(d), the relatively small-scale vortices distribute in all the measured region, especially near the wall. A part of them is contained in large- or intermediate-scale flow structures.

Figure 15 shows the measured instantaneous streamlines and multiscale streamlines with the contours of the spanwise vorticity $\omega_y D/U$ in the (x, z) plane at $y/D = 0$, which are extracted from Fig. 14. The instantaneous measured streamlines and their contours of the streamwise vorticity [Fig. 15(a)] exhibit a large separation vortex and several smaller vortices. This large vortex is formed by the interaction between the free end downwash flow and upwash flow from the ground plane, which can also be observed in the time-averaged 3D flow structure of Fig. 7. The large-scale instantaneous streamlines with its contours of the streamwise vorticity $\omega_{y1} D/U$ at the wavelet level 1 (with the central scale of $a/D = 0.55$), as indicated in Fig. 15(b), evidently display the large-scale separation vortex.

Figure 15(c) plotted the instantaneous intermediate-scale contours of the streamwise vorticity $\omega_{y2} D/U$ at the wavelet level 2 having the central scale of $a/D = 0.27$. Some intermediate-scale strong vortices, which represent the frag-

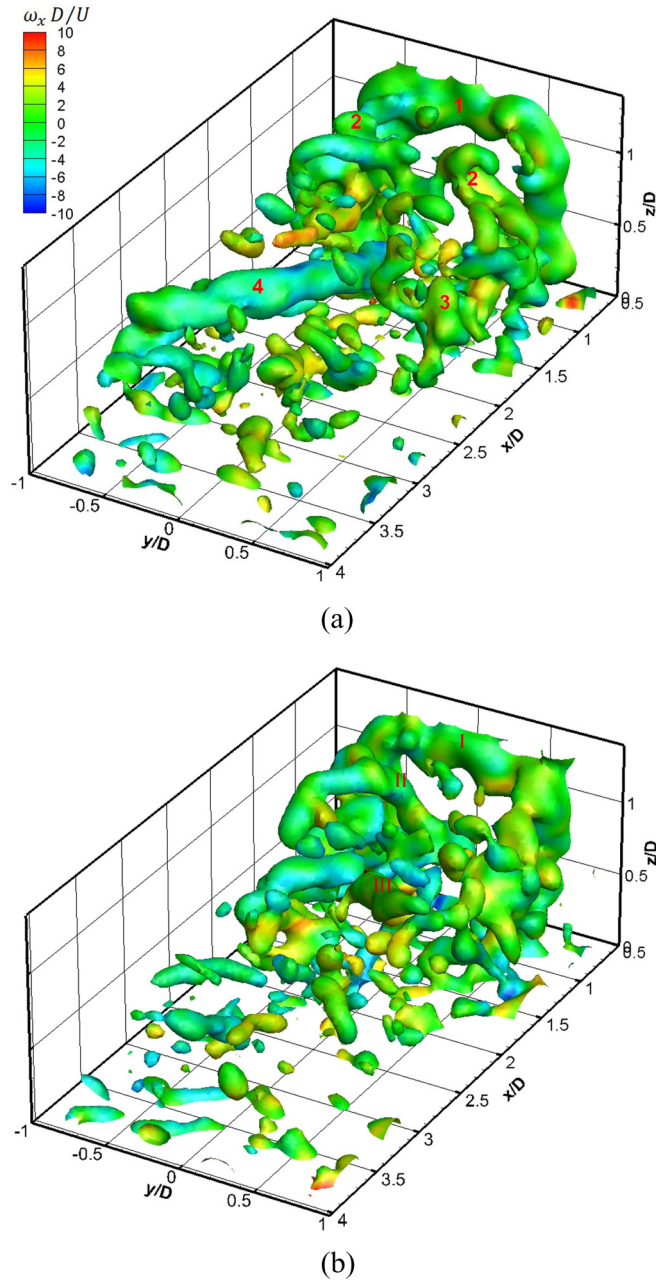


FIG. 12. The instantaneous isosurfaces of $Q/(U/D)^2 = 2.5$ colored by the streamwise vorticity $\omega_x D/U$. (a) t_0 . (b) $t_0 + 12s$.

ments of W-type arch vortices and trailing vortices as indicated by arrows in Fig. 15(c), are extracted. These relatively strong vortices also correspond to the measured flow structures of Fig. 15(a).

As to the small scale of the wavelet level 3 with the central scale of $a/D = 0.14$, the relatively small-scale vortices distribute behind cylinder and near the bottom plate. Several strong vortices, as pointed by arrows in Fig. 15(d), are also observed in Fig. 15(a) or are contained in intermediate-scale structures of Fig. 15(c), which represents active small-scale vortices.

Figure 16(a) shows the measured instantaneous streamlines and contours of the normalized vorticity $\omega_z D/U$ in the $(x,$

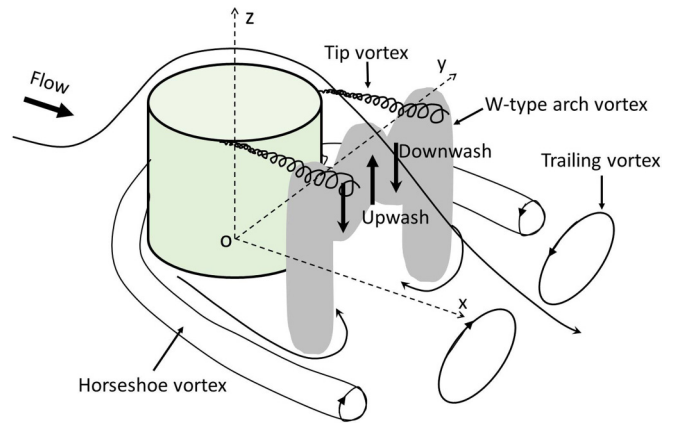


FIG. 13. Sketch of the time-averaged flow field around a short circular cylinder.

$y)$ plane at the longitudinal positions of $z/D = 0.5$. The two instantaneous longitudinal large vortices shedding from the two side walls of the cylinder are clearly observed even they are not same size, which act as legs of the arch vortex. Meanwhile several smaller vortices appear in the shear layer. Figure 16(b) exhibits the large-scale instantaneous streamlines and contours of the longitudinal vorticity $\omega_z D/U$ for the wavelet level 1. A pair of the almost symmetric large-scale vortex is extracted, which corresponds to the vortices in Fig. 16(a). However, the size of large-scale vortices in the (x, y) plane decreases and vorticity strength increases with z/D . It is inferred that such a phenomenon results in the interaction between the shedding vortex of the side wall and the tip vortex of the free end.

The intermediate-scale flow structures of wavelet level 2 are plotted in Fig. 16(c). It is evident that intermediate-scale vortices dominate the flow field in the (x, y) plane of $z/D = 0.5$. They may be fragments of W-type arch vortices, tip vortices, and trailing vortices, which are different from that in the (x, z) plane. The stronger vortices shedding from the two side walls of the cylinder are extracted around $y/D = \pm 0.5$ near the cylinder, which correspond to the measured flow structures of Fig. 16(a).

As decreasing to the small scale in Fig. 16(d), although the instantaneous small-scale vortices distribute in all measured regions, the small-scale vortices exhibit the highest vorticity near the two side walls of the cylinder. These small-scale vortices are contained in the intermediate-scale flow structures of wavelet level 2. Meanwhile, the small-scale vortices are the most active in the (x, y) plane of $z/D = 0.2$ (not shown here) because this plane is close to the ground plane and horseshoe and base vortices are presented.

Figure 17 shows the measured instantaneous streamlines and contours of the dimensionless streamwise vorticity $\omega_x D/U$ in the (y, z) plane at the downstream locations of $x/D = 1.1, 1.5, 2.0,$ and 2.6 . Here the black dotted line indicates the location of the short cylinder. At the downstream of $x/D = 1.1$, a positive tip vortex and a negative tip vortex, produced from the trailing edge of the free end, are clearly observed near the upper corners of the free end. Between the tip vortex pair, the upwash and downwash flows are

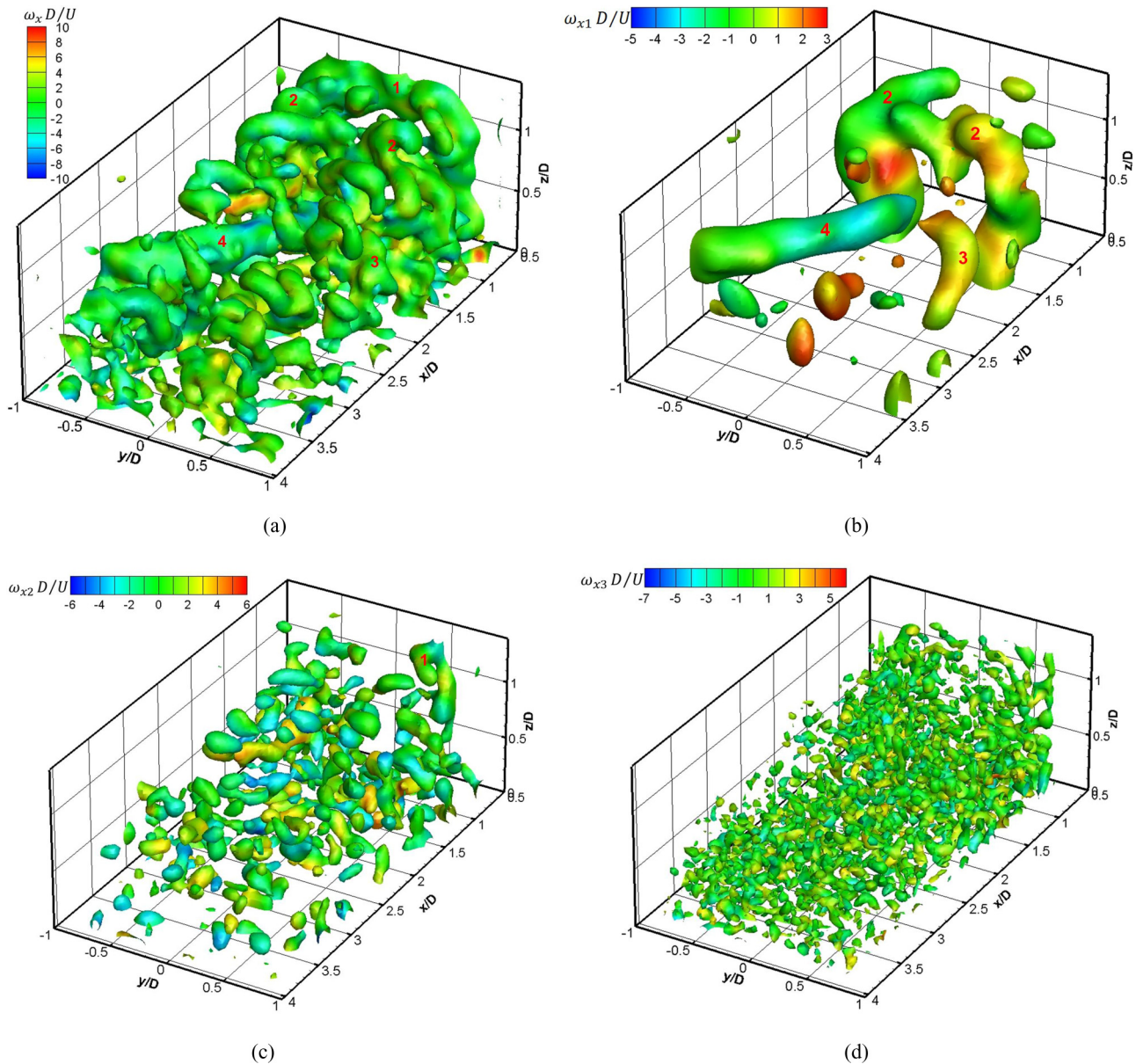


FIG. 14. The instantaneous multiscale isosurface of $Q_i/(U/D)^2 = 1$ colored by the streamwise vorticity $\omega_{xi}D/U$. (a) Measured. (b) Level 1. (c) Level 2. (d) Level 3.

clearly found near the height of the short cylinder, and a large-scale streamwise vortex is originated near the position of the cylinder center, which is an important reason of forming instantaneous W-type head of arch vortex. A instantaneous base vortex pair is also identified near the connection between cylinder and ground plane.

At the location of $x/D = 1.5$, this tip vortex pair moves towards the ground plane because of the downwash effect. The shedding vortices from two side walls begin to incline due to the effect of upward and downwash flows. The strength of the large-scale streamwise vortex increases because of the interaction between the downwash flow and shedding vortices, which is evident observed at $x/D = 2.0$ and 2.6 . The 3D structure of this large-scale streamwise vortex is labeled by 4 in Fig. 12. Otherwise, several relatively smaller vortices are observed near the bottom plate. At the downstream of $x/D =$

2.0 and 2.6 , the sizes of these relatively smaller vortices increase and become two large vortices at $x/D = 2.6$.

Figures 18–20 show the multiscale instantaneous streamlines and contours of the dimensionless streamwise vorticity $\omega_{xi}D/U$ in the (y, z) plane at $x/D = 1.1, 1.5, 2.0,$ and 2.6 , which are extracted from 3D wavelet multiresolution analysis of the measured instantaneous 3D velocity data (Fig. 12). As shown in Fig. 18(a), a tip vortex pair near the upper corners of the free end appears in the large-scale flow structure at $x/D = 1.1$, which corresponds to the measured flow structures [Fig. 18(a)]. At the downstream of $x/D = 1.5$, besides the tip vortex pair, strong negative and weak positive streamwise vortices appear and develop from $x/D = 1.5–2.6$. It implies that the strong large-scale downwash interacts with shedding vortices of the side wall from $x/D = 1.5–2.6$ and originates the large-scale streamwise vortex, which cannot be clearly ob-

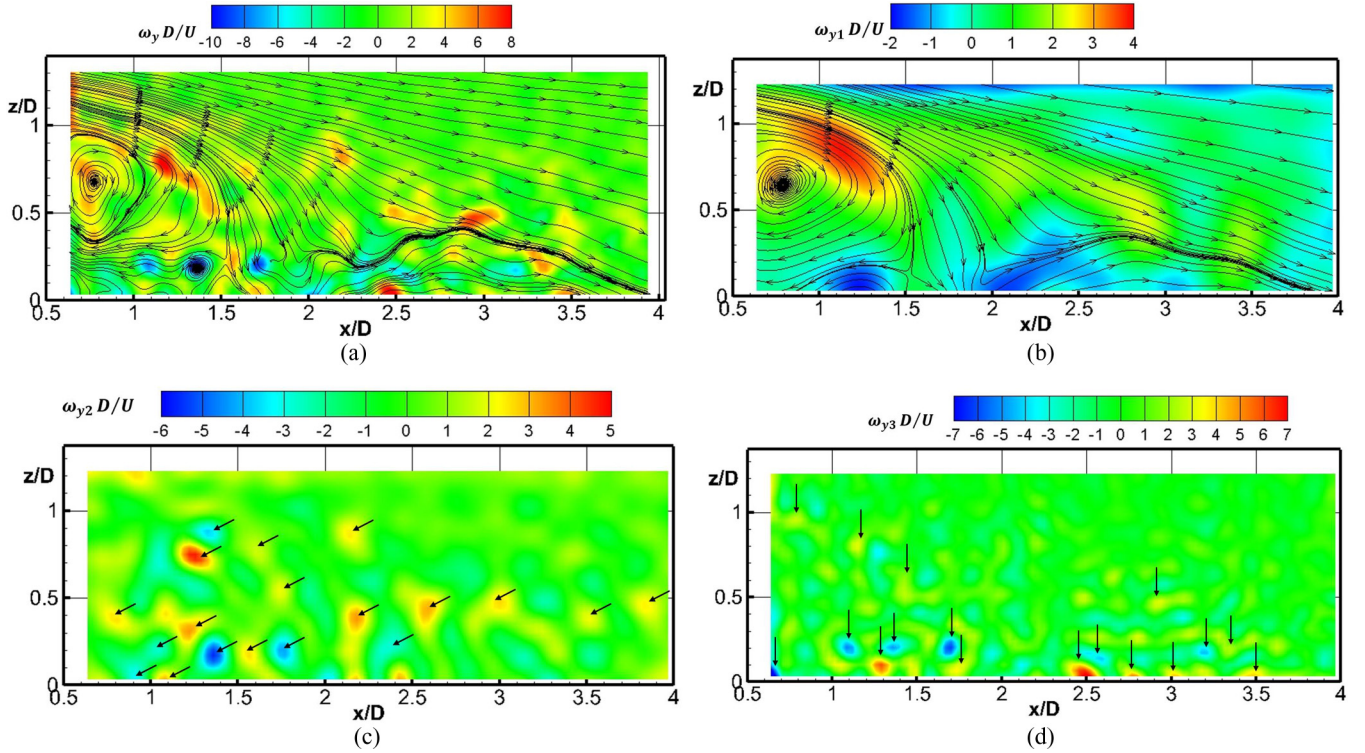


FIG. 15. The instantaneous multiscale streamlines and contours of the spanwise vorticity $\omega_y D/U$ in the (x, z) plane of $y/D = 0$. (a) Measured. (b) Level 1. (c) Level 2. (d) Level 3.

served from the measured data of Fig. 17. At the downstream of $x/D = 2.6$, two strong large-scale streamwise vortices dominate the flow structures. However, the tip vortex starts to decay.

Figure 19 shows the instantaneous intermediate-scale flow structures in the (y, z) plane at $x/D = 1.1, 1.5, 2.0$, and 2.6 . It is evident that each large-scale streamwise vortex contains several intermediate-scale vortices distributed around the cylinder region. Some vortices, which couldn't be observed at the wavelet level 1, are extracted from the measured data at the wavelet level 2. At the location of $x/D = 1.1$, the low concentrations of intermediate-scale vortices are observed, in which a pair of base vortices [Fig. 17(a)] are identified as the intermediate-scale vortices. Especially, a vortex is clearly observed around $y/D = 0$ and $z/D = 1$ (the trailing edge of the free end surface), which may cause the upwash flow. It plays an important role in originating a W-type head of the arch vortex. At locations of $x/D = 1.5$ and 2.0 , the strength of intermediate-scale vortices increases. Except for the large-scale streamwise vortex, all vortices appearing in the measured flow structures of Fig. 17(b) are found at the wavelet level 2, implying that the intermediate-scale vortices dominate the flow structures at this location. However, the intermediate-scale streamwise vortices begin to decay from the downstream of $x/D = 2.6$, and the relatively strong intermediate-scale vortices exist in the two large-scale streamwise vortices [Fig. 18(d)].

The instantaneous small-scale flow structures in the (y, z) plane at $x/D = 1.1, 1.5, 2.0$, and 2.6 are shown in Fig. 20. It is observed that most of the small-scale vortices are contained in the intermediate-scale flow structures and distributed around

the cylinder region. The small-scale vortices first increase along the downstream direction due to the breaking down of the large- and intermediate-scale vortices, and then decrease after $x/D = 2.0$. At $x/D = 1.5$ the relatively strong vortices appear in the shear layer or near the bottom plate, which indicates the strong interaction between the shedding vortices and downwash flow near the separation point [Fig. 9(a)].

V. TIME-AVERAGED 3D MULTISCALE WAKE STRUCTURES

In order to extract the time-mean multiscale wake structures, time serial instantaneous large- and intermediate-scale velocity fields of 400 snapshots, which are obtained by 3D wavelet multiresolution analysis of Tomo-PIV data, are respectively averaged. Figure 21 shows the time-averaged large- and intermediate-scale $Q_i/(U/D)^2$ isosurface with colored by the time-averaged streamwise vorticity $\bar{\omega}_{xi}D/U$. Here $i = 1$ and 2 represents the wavelet level 1 and 2, respectively. As shown in Fig. 21(a), the large-scale structure exhibits a large 3D arch vortex of M shape [23] behind the short cylinder. A pair of tip vortices around two convex parts near the two sides of the horizontal part of the arch vortex is also clearly observed. However, the large-scale streamwise vortices, which are observed in the instantaneous large-scale structures of Fig. 14(b), disappear in the time-averaged large-scale structure of level 1.

In the intermediate-scale structure, as indicated in Fig. 21(b), a W-type head-shaped arch structure standing on the ground plane behind the short cylinder is evident, which is the strong arch vortex structure. Besides a tip vortex pair,

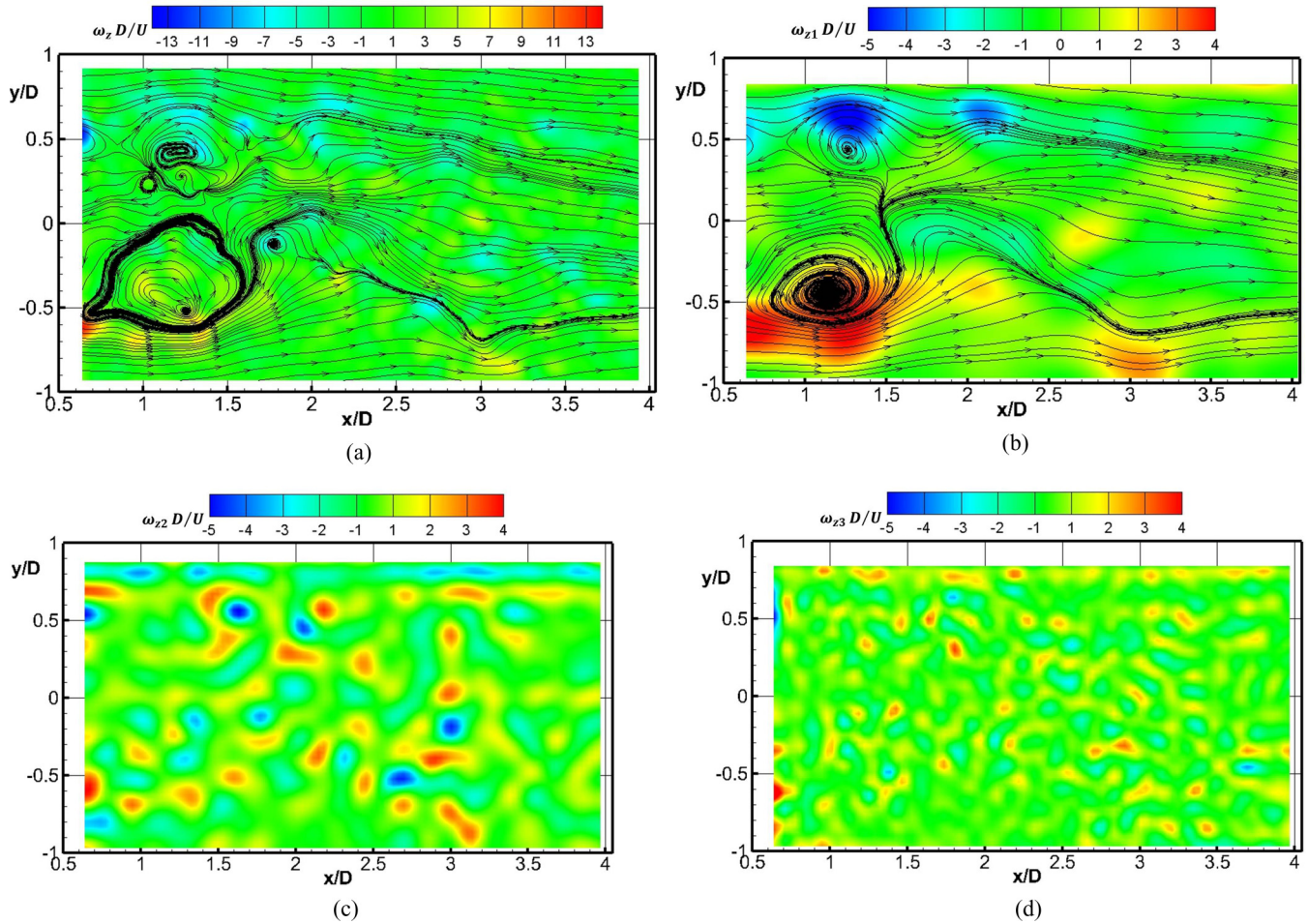


FIG. 16. The instantaneous multiscale streamlines and contours of the longitudinal vorticity $\omega_z D/U$ in the (x, y) plane of $z/D = 0.5$. (a) Measured. (b) Level 1. (c) Level 2. (d) Level 3.

another vortex pair is evidently observed near the center convex of the horizontal part on the W-type arch structure, which is induced by the strong upwash flow and forms a W-type head shape. Several intermediate-scale streamwise vortices also appear at the downstream.

As discussed above, the strong W-type head-shaped arch structure, which is an intermediate-scale structure, develops the large-scale arch structure of an M shape [23]. The tip vortices simultaneously exist in the large- and intermediate-scale structures.

VI. CONCLUSIONS

To clarify the 3D multiscale flow structures behind a wall-mounted short cylinder, the Tomo-PIV measurements were carried out and 3D wavelet transform were applied to analyze Tomo-PIV data in this study. The main results are shown as follows.

(1) A strong 3D W-type arch vortex was first found behind short cylinder. The “head” of the horizontal part was induced by the upwash flow of the large-scale flow separation, and the “shoulders” of the horizontal part were caused by the downward flow and tip vortices. At the downstream, the 3D W-type arch vortex was reshaped to the M-shaped arch vortex and then broke down into several fragments.

(2) The large-scale streamwise vortices were originated by the downwash and upwash flows near the center location of the W-type arch vortex and were connected with fragments of the arch vortices or shedding vortices of the side wall.

(3) The horizontal shape of the arch vortex structure depended on the aspect ratio of cylinder.

(4) The instantaneous arch vortex was extracted at the wavelet level 1. Downstream, two strong large-scale streamwise vortices dominated the flow structures in the near wake.

(5) The instantaneous intermediate-scale upwash vortices played an important role in inducing the W-type head of the arch vortex. The instantaneous intermediate-scale streamwise vortices and trailing vortices were also extracted at the wavelet level 2.

(6) Relatively strong small-scale vortices appeared in the shear layer or near the bottom plate and the small-scale structures were mostly contained in the intermediate-scale structures.

(7) The W-type head-shaped arch vortex was extracted in the time-mean intermediate-scale structure, and an M-shaped arch vortex was found in the time-mean large-scale structure.

(8) The tip vortices were distributed in the time-mean large- and intermediate-scale structures.

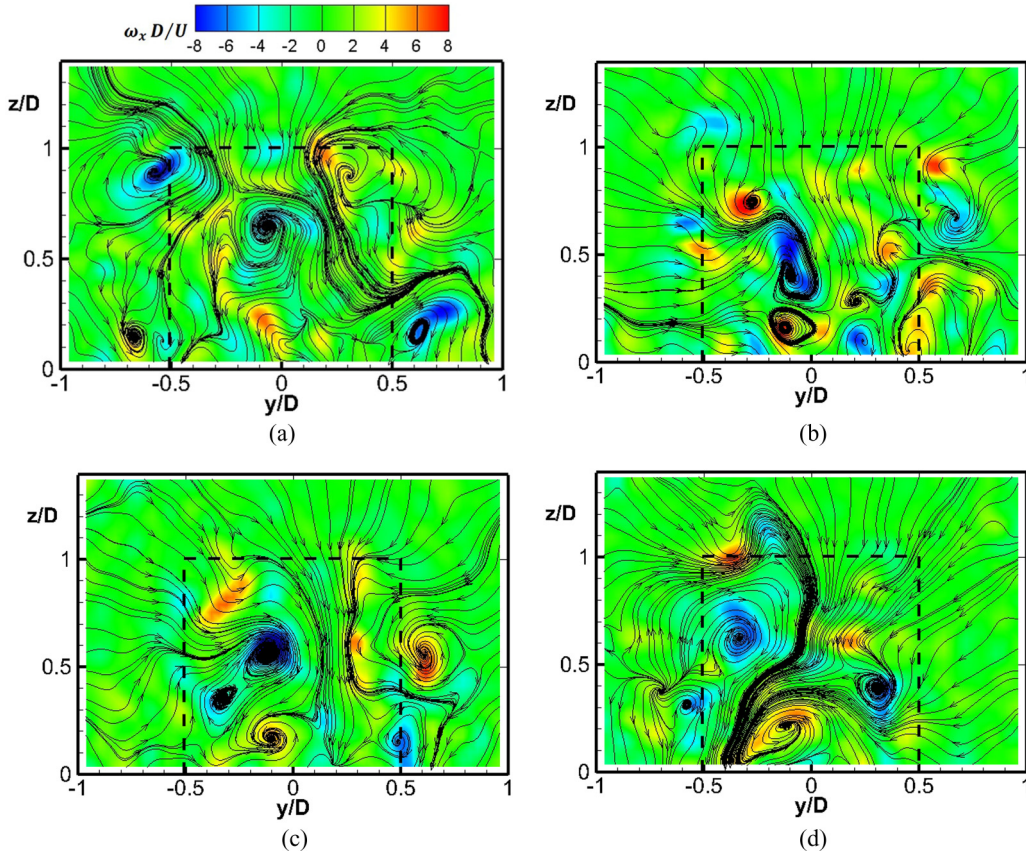


FIG. 17. The measured streamlines and contours of the streamwise vorticity $\omega_x D/U$ in the (y, z) plane. (a) $x/D = 1.1$. (b) $x/D = 1.5$. (c) $x/D = 2.0$. (d) $x/D = 2.6$.

ACKNOWLEDGMENTS

The authors wish to acknowledge the following financial support: Research Fellowships for Young Scientists (2019–2022), Grant-in-Aid for JSPS Fellows (Grant No. 19J20739), Grant-in-Aid for Scientific Research (C) (Grant No. 20K04257) from JSPS, and National Natural Science Foundation of China (Grants No. 11721202 and No. 11772035) from Beihang University. The authors also wish to acknowledge Dr. C.Y. Wang, Dr. H.Y. Zhu, and X.L. Han, Beihang University, for their help in the tomographic PIV experiments.

APPENDIX: 3D ORTHOGONAL WAVELET TRANSFORM

Wavelet transform is classified into discrete (orthogonal) and continuous wavelet transforms for capturing local features of data in the spatial-scale plane. A continuous spatial-scale identification of data may be realized by the continuous wavelet transform. The wavelet coefficients of orthogonal wavelet transform exhibit the local features of data in spatial and scale bands. However, the wavelet coefficients of each scale band are orthogonal independent of each other. The orthogonal wavelet transform provides enough spatial resolution in the small-scale ranges and low spatial resolution in the large-scale range. Therefore, the limitations of conventional

bandpass transform are overcome. Furthermore, the orthogonal wavelet transform is reversible so that the measured data can be uniquely reconstructed based on a wavelet basis function selected from the inversely transformed wavelet coefficients. Previous studies have described 1D and 2D orthogonal wavelet transforms [1,35], and this section states the definition of 3D orthogonal wavelet transform briefly [29].

For a 3D velocity data $V^N = [v_{i,j,k}]$ ($i = 1, \dots, 2^N$; $j = 1, \dots, 2^N$; $k = 1, \dots, 2^N$), which is a matrix of $2^N \times 2^N \times 2^N$, its 3D wavelet transform is based on an orthogonal Daubechies wavelet basis ($2^N \times 2^N$ matrix C^N), for example Daubechies wavelet basis with an order of 12. The matrix C^N acts as a smoothing (low-pass) filter and a difference (high-pass) filter. The rank of square matrix C^N is N since it is a nonsingular matrix.

The 3D wavelet transform is performed by transforming the array sequentially on its first index (for all values of its other indices), then on its second index, and last on its third index, i.e., operating the 1D wavelet transform sequentially in the horizontal, vertical, and longitudinal directions.

The following describe the operations: As the wavelet transform of the first level, the data array of the horizontal direction (x direction) $V_{j,k}^N$ ($j = 1, \dots, 2^N$; $k = 1, \dots, 2^N$) is carried out by multiplying the wavelet basis matrix C^N and a permuting matrix P^N at first step; we obtain the first wavelet

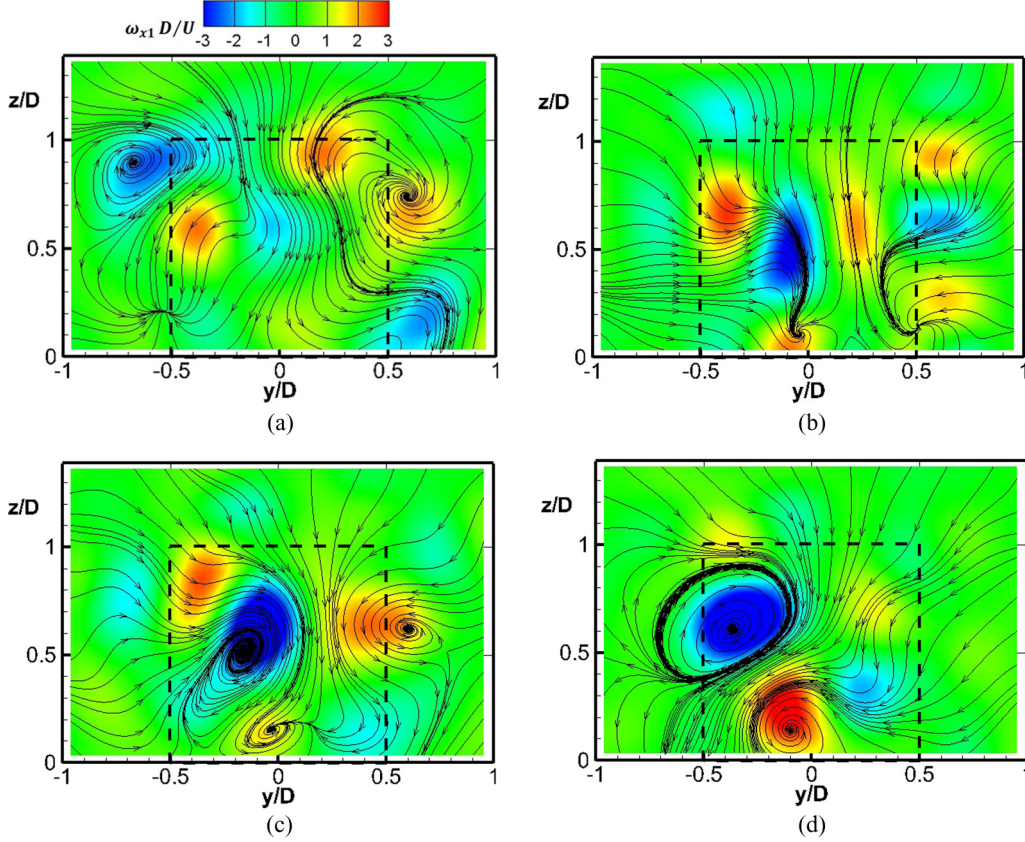


FIG. 18. The larger-scale streamlines and contours of the streamwise vorticity $\omega_{x1}D/U$ in the (y, z) plane. (a) $x/D = 1.1$. (b) $x/D = 1.5$. (c) $x/D = 2.0$. (d) $x/D = 2.6$.

coefficients \mathbf{V}^N along the x direction as

$${}^1\mathbf{V}_{j,k}^x = \mathbf{P}^N \times \mathbf{C}^N \times \mathbf{V}_{j,k} \quad (j = 1, \dots, 2^N; k = 1, \dots, 2^N). \quad (\text{A1})$$

The resulting first transform coefficient matrix, ${}^1\mathbf{V}_{j,k}^x$, is composed of interlaced smooth and difference coefficients. At this step, the even rows of the matrix are moved backward as the last 2^{N-1} elements (difference coefficients) and the odd rows of the matrix are moved forward as the first 2^{N-1} elements (smooth coefficients).

The second step is to divide the 3D matrix ${}^1\mathbf{V}_{i,j,k}^x$ ($i = 1, \dots, 2^N$; $j = 1, \dots, 2^N$; $k = 1, \dots, 2^N$) [Eq. (A1)] into two block matrices, ${}^1\mathbf{V}_{i,k}^{xs}$ and ${}^1\mathbf{V}_{i,k}^{xd}$ ($i = 1, \dots, 2^{N-1}$; $k = 1, \dots, 2^N$). By multiplying with the wavelet basis matrix \mathbf{C}^N and the permuting matrix \mathbf{P}^N along the y direction, the above two block matrices are transferred as

$${}^1\mathbf{V}_{i,k}^{xys} = \mathbf{P}^N \times \mathbf{C}^N \times {}^1\mathbf{V}_{i,k}^{xs}, \quad (\text{A2a})$$

$${}^1\mathbf{V}_{i,k}^{xyd} = \mathbf{P}^N \times \mathbf{C}^N \times {}^1\mathbf{V}_{i,k}^{xd}$$

$$(i = 1, \dots, 2^{N-1}; k = 1, \dots, 2^N). \quad (\text{A2b})$$

Therefore, we obtain the 3D matrix ${}^1\mathbf{V}^{xy}$ by transformation along the x and y directions, which consists of the following four block matrices: ${}^1\mathbf{V}_{i,j}^{xys}$, ${}^1\mathbf{V}_{i,j}^{xyd}$, ${}^1\mathbf{V}_{i,j}^{xysd}$, ${}^1\mathbf{V}_{i,j}^{xydd}$ ($i = 1, \dots, 2^{N-1}$; $j = 1, \dots, 2^{N-1}$).

At the third step, along the z direction the above four block matrices are decomposed by the wavelet basis matrix \mathbf{C}^N and

the permuting matrix \mathbf{P}^N into

$${}^1\mathbf{V}_{i,j}^{xyzss} = \mathbf{P}^N \times \mathbf{C}^N \times {}^1\mathbf{V}_{i,j}^{xys}, \quad (\text{A3a})$$

$${}^1\mathbf{V}_{i,j}^{xyzsd} = \mathbf{P}^N \times \mathbf{C}^N \times {}^1\mathbf{V}_{i,j}^{xyd}, \quad (\text{A3b})$$

$${}^1\mathbf{V}_{i,j}^{xyzds} = \mathbf{P}^N \times \mathbf{C}^N \times {}^1\mathbf{V}_{i,j}^{xysd}, \quad (\text{A3c})$$

$${}^1\mathbf{V}_{i,j}^{xyzdd} = \mathbf{P}^N \times \mathbf{C}^N \times {}^1\mathbf{V}_{i,j}^{xydd}$$

$$(i = 1, \dots, 2^{N-1}; j = 1, \dots, 2^{N-1}). \quad (\text{A3d})$$

Finally, the following eight block matrices consist of the first wavelet transform coefficients of the matrix: $\mathbf{V}^N: {}^1\mathbf{V}_{i,j,k}^{xyzsss}$, ${}^1\mathbf{V}_{i,j,k}^{xyzsds}$, ${}^1\mathbf{V}_{i,j,k}^{xyzdss}$, ${}^1\mathbf{V}_{i,j,k}^{xyzdds}$, ${}^1\mathbf{V}_{i,j,k}^{xyzssd}$, ${}^1\mathbf{V}_{i,j,k}^{xyzsdd}$, ${}^1\mathbf{V}_{i,j,k}^{xyzdsd}$, and ${}^1\mathbf{V}_{i,j,k}^{xyzddd}$ ($i = 1, \dots, 2^{N-1}$; $j = 1, \dots, 2^{N-1}$; $k = 1, \dots, 2^{N-1}$). Here ${}^1\mathbf{V}_{i,j,k}^{xyzsds}$, ${}^1\mathbf{V}_{i,j,k}^{xyzdss}$, ${}^1\mathbf{V}_{i,j,k}^{xyzdds}$, ${}^1\mathbf{V}_{i,j,k}^{xyzssd}$, ${}^1\mathbf{V}_{i,j,k}^{xyzsdd}$, ${}^1\mathbf{V}_{i,j,k}^{xyzdsd}$, and ${}^1\mathbf{V}_{i,j,k}^{xyzddd}$ are the wavelet coefficients of level 1.

The wavelet transform of the second level is performed to the smooth block matrices of ${}^1\mathbf{V}_{i,j,k}^{xyzsss}$ ($i = 1, \dots, 2^{N-1}$; $j = 1, \dots, 2^{N-1}$; $k = 1, \dots, 2^{N-1}$) based on the wavelet basis matrix \mathbf{C}^{N-1} and the permuting matrix \mathbf{P}^{N-1} , which are the halves of \mathbf{C}^N and \mathbf{P}^N , respectively. Along x , y , and z directions in a similar way to the first level transform, the wavelet transform coefficients of level 2 are obtained.

The pyramidal computation is operated until the matrix of the last wavelet level only consists of $2^3 \times 2^3 \times 2^3$ elements.

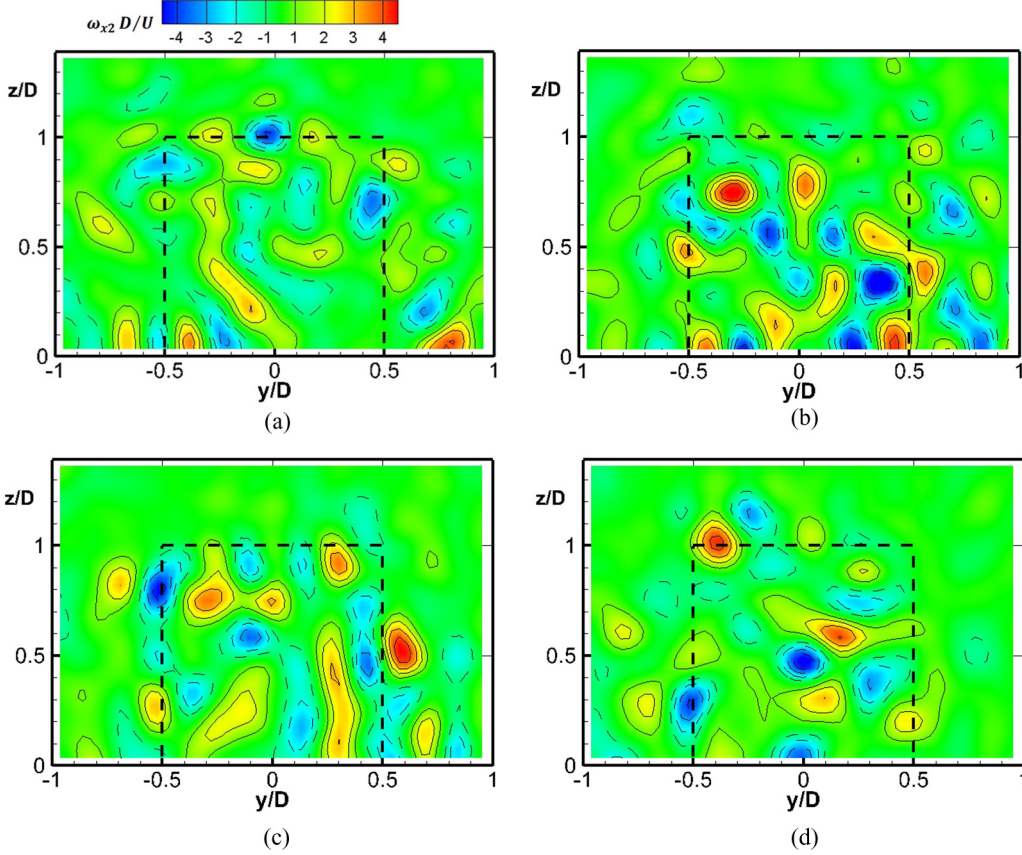


FIG. 19. The intermediate-scale contours of the streamwise vorticity $\omega_{x2}D/U$ in the (y, z) plane. (a) $x/D = 1.1$. (b) $x/D = 1.5$. (c) $x/D = 2.0$. (d) $x/D = 2.6$.

At last the 3D wavelet coefficients S is written as

$$S = (W(W(WV^N)^T)^T)^T, \quad (\text{A4})$$

where W is produced based on the orthogonal wavelet basis matrix C^N and the permuting matrix P^N in the processing of a pyramidal algorithm of orthogonal wavelet transformation:

$$W = P^4 C^4 \dots P^{N-1} C^{N-1} P^N C^N. \quad (\text{A5})$$

Here W satisfies $W^T W = I$, where I is a unit matrix. It indicates that the 3D discrete wavelet transform is an orthogonal linear operator and invertible. We may perform the inverse orthogonal wavelet transform by reversing the procedure as follows:

$$V^N = W^T W^T S^T W. \quad (\text{A6})$$

Being similar to 1D and 2D wavelet multiresolution techniques, the orthogonal wavelet coefficient of matrix S is first resolved into the following sum of all levels:

$$S = D_1^N + D_2^N + \dots + D_{N-2}^N, \quad (\text{A7})$$

where D_i^N , having a size of $2^N \times 2^N \times 2^N$, is composed of a zero matrix and a coefficient matrix at wavelet level i .

Then we apply the inverse orthogonal wavelet transform to the wavelet coefficients, viz.

$$V^N = W^T W^T D_1^T W + W^T W^T D_2^T W + \dots + W^T W^T D_i^T W + \dots + W^T W^T D_{N-2}^T W. \quad (\text{A8})$$

Here the first term $W^T W^T D_1^T W$ and the last term $W^T W^T D_{N-2}^T W$ indicate the components of wavelet level 1 (the highest grouped frequency) and level $N - 2$ (the lowest grouped frequency), respectively. It is evident that the original data can be reconstructed from the sum of all wavelet components by using the orthogonal wavelet bases. Such decomposition process is called as the *three-dimensional wavelet multiresolution technique*. By using this method, the flow structures are decomposed into several wavelet components depended on their central frequencies, which are the different scale flow structures.

For considering the effect of orthogonal wavelet basis, some orthogonal wavelet functions (Daubechies, Harmonic, LMB, and Meyer) were used by Mouri *et al.* [46]. They suggested that the statistics of turbulent flow were insensitive to the choice of the wavelets. Our previous study [47] also pointed out that the results of the wavelet multiresolution analysis are essentially independent of the choice of wavelet basis having an order higher than 10. In this study, the Daubechies wavelet base with an order of 20 is chosen as the orthogonal wavelet basis.

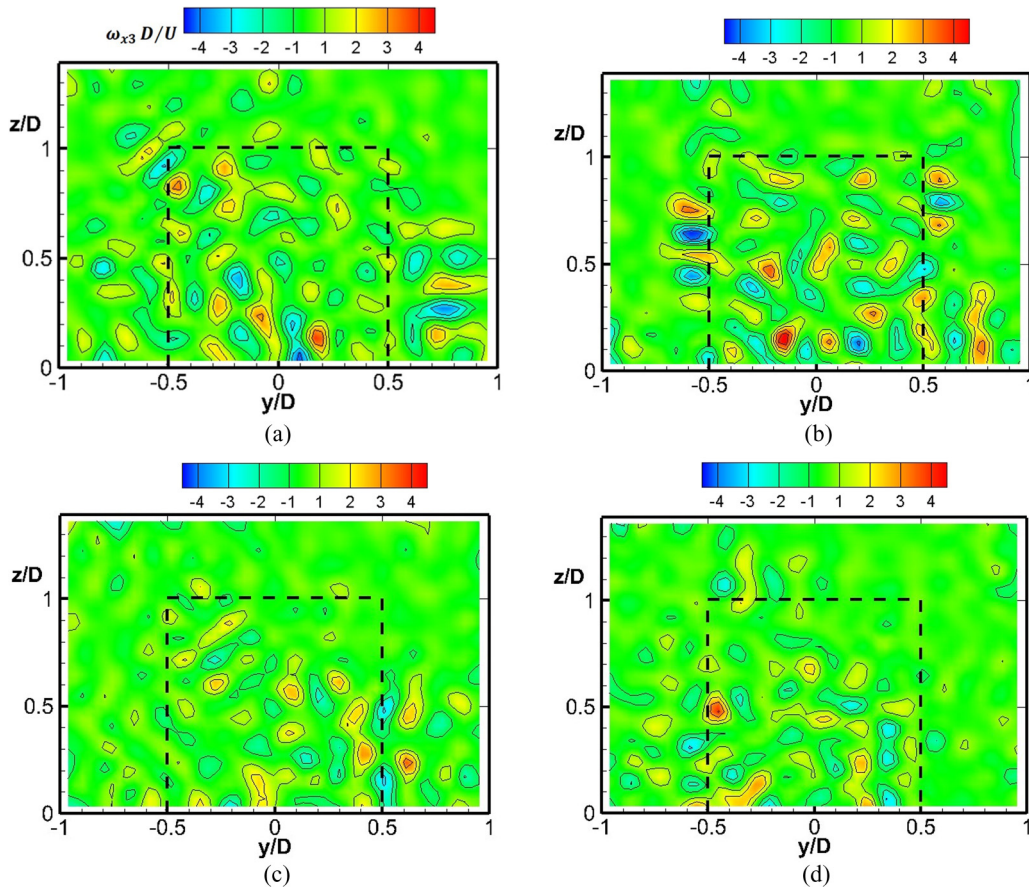


FIG. 20. The small-scale contours of the streamwise vorticity $\omega_{x3} D/U$ in the (y, z) plane. (a) $x/D = 1.1$. (b) $x/D = 1.5$. (c) $x/D = 2.0$. (d) $x/D = 2.6$.

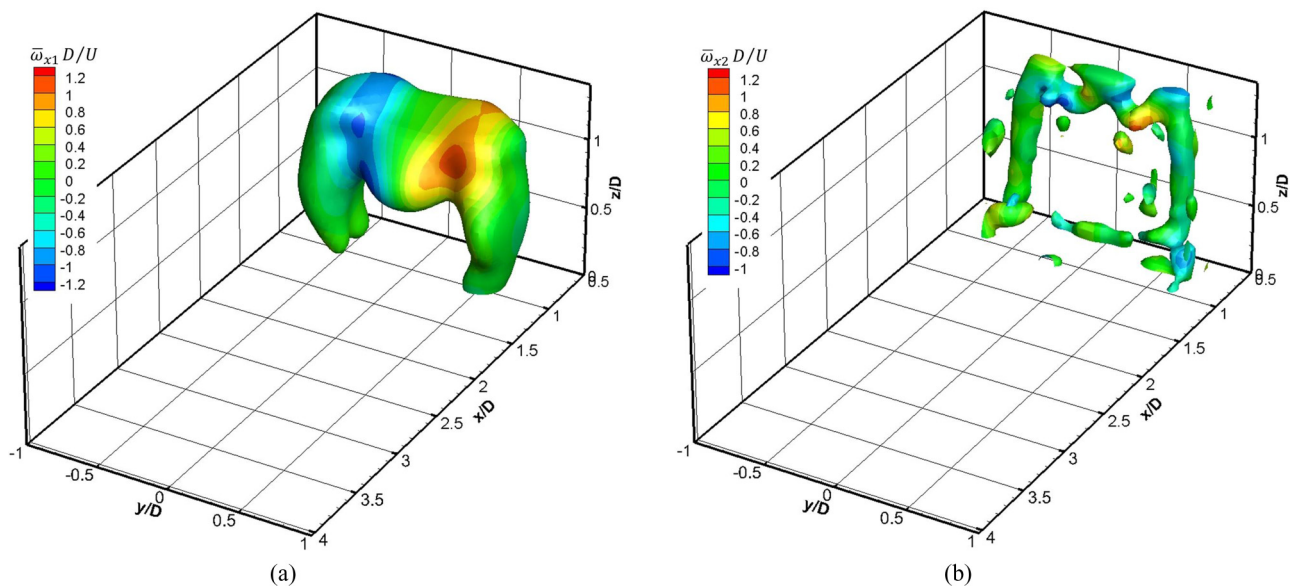


FIG. 21. The time-averaged large- and intermediate-scale isosurface of $Q_i/(U/D)^2$ colored by the streamwise vorticity $\bar{\omega}_{xi} D/U$. (a) Level 1 ($Q_1/(U/D)^2 = 0.7$). (b) Level 2 ($Q_2/(U/D)^2 = 0.15$).

- [1] A. Rinoshika and Y. Zhou, Orthogonal wavelet multi-resolution analysis of a turbulent cylinder wake, *J. Fluid Mech.* **524**, 229 (2005).
- [2] A. Rinoshika and Y. Zhou, Reynolds number effects on wavelet components of self-preserving turbulent structures, *Phys. Rev. E* **79**, 046322 (2009).
- [3] D. Sumner, J. L. Heseltine, and O. J. P. Dansereau, Wake structure of a finite circular cylinder of small aspect ratio, *Exp. Fluids* **37**, 720 (2004).
- [4] R. J. Pattenden, S.R. Turnock, and X. Zhang, Measurements of the flow over a low-aspect-ratio cylinder mounted on a ground plane, *Exp. Fluids* **39**, 10 (2005).
- [5] H. F. Wang and Y. Zhou, The finite-length square cylinder near wake, *J. Fluid Mech.* **638**, 453 (2009).
- [6] R. T. Gonçalves, G. R. Franzini, G. F. Rosetti, J. R. Meneghini, and A. L. C. Fajarra, Flow around circular cylinders with very low aspect ratio, *J. Fluids Struct.* **54**, 122 (2015).
- [7] S. Tanaka and S. Murata, An investigation of the wake structure and aerodynamic characteristics of a finite circular cylinder, *JSME Int. J., Ser. B* **42**, 178 (1999).
- [8] T. Kawamura, M. Hiwada, T. Hibino, T. Mabuchi, and M. Kumada, Flow around a finite circular cylinder on a flat plate, *Bull. JSME* **27**, 2142 (1984).
- [9] C. R. Johnston and D. J. Wilson, A vortex pair model for plume downwash into stack wakes, *Atmos. Environ.* **31**, 13 (1996).
- [10] M. S. Adaramola, O. J. Akinlade, D. Sumner, D. J. Bergstrom, and A. J. Schenstead, Turbulent wake of a finite circular cylinder of small aspect ratio, *J. Fluids Struct.* **22**, 919 (2006).
- [11] L. W. Lee, Wake structure behind a circular cylinder with a free end, In: Proc. Heat Transfer Fluid Mech. Inst. **35**, 241 (1997).
- [12] T. Okamoto and M. Yagita, The experimental investigation on the flow past a circular cylinder of finite length placed normal to the plane surface in a uniform stream, *Bull. JSME* **16**, 805 (1973).
- [13] T. Kawamura, M. Hiwada, T. Hibino, T. Mabuchi, and M. Kumada, Flow around a finite circular on flat plate: in the case of cylinder length larger than turbulent boundary layer thickness, *Trans. JSME* **50**, 332 (1984) (in Japanese).
- [14] S. C. Roh and S. O. Park, Vortical flow over the free end surface of a finite circular cylinder mounted on a flat plate, *Exp. Fluids* **34**, 63 (2003).
- [15] S. Krajnović, Flow around a tall finite cylinder explored by large eddy simulation, *J. Fluid Mech.* **676**, 294 (2011).
- [16] N. Rostamy, D. Sumner, D. J. Bergstrom, and J. D. Bugg, Local flow field of a surface-mounted finite circular cylinder, *J. Fluids Struct.* **34**, 105 (2012).
- [17] D. Sumner, Flow above the free end of a surface-mounted finite-height circular cylinder, A review, *J. Fluids Struct.* **43**, 41 (2013).
- [18] R. Porteous, D. J. Moreau, and C. J. Doolan, A ref flow-induced noise from finite wall-mounted cylinders, *J. Fluids Struct.* **51**, 240 (2014).
- [19] H. Rinoshika, A. Rinoshika, and S. Fujimoto, Passive control on flow structure around a wall-mounted low aspect ratio circular cylinder by using an inclined hole, Bulletin of the JSME, *J. Fluid Sci. Technol.* **12**, JFST0006 (2017).
- [20] H. Rinoshika and A. Rinoshika, Effect of a horizontal hole on flow structures around a wall-mounted low-aspect-ratio cylinder, *Int. J. Heat Fluid Flow* **71**, 80 (2018).
- [21] H. Rinoshika, A. Rinoshika, and S. Fujimoto, Visualization of a finite wall-mounted cylinder wake controlled by a horizontal or inclined hole, *J. Visualization* **21**, 543 (2018).
- [22] H. Rinoshika and A. Rinoshika, Passive control of a front inclined hole on flow structures around a surface-mounted short cylinder, *Ocean Eng.* **189**, 106383 (2019).
- [23] H. Y. Zhu, C. Y. Wang, H. P. Wang, and J. J. Wang, Tomographic PIV investigation on 3D wake structures for flow over a wall-mounted short cylinder, *J. Fluid Mech.* **831**, 743 (2017).
- [24] C. Meneveau, Analysis of turbulence in the orthonormal wavelet representation, *J. Fluid Mech.* **232**, 469 (1991).
- [25] M. Yamada and K. Ohkitani, An identification of energy cascade in turbulence by orthonormal wavelet analysis, *Prog. Theor. Phys.* **86**, 799 (1991).
- [26] M. Farge, Wavelet transforms and their applications to turbulence, *Annu. Rev. Fluid Mech.* **24**, 395 (1992).
- [27] M. Farge, N. Kevlahan, V. Perrier, and E. Goirand, Wavelets and Turbulence, *Proc. IEEE* **84**, 639. (1996).
- [28] K. Schneider and O. V. Vasilyev, Wavelet methods in Computational Fluid Dynamics, *Annu. Rev. Fluid Mech.* **42**, 473 (2010).
- [29] A. Rinoshika and H. Rinoshika, Application of multi-dimensional Wavelet Transform to Fluid Mechanics, *Theor. Appl. Mech. Lett.* **10**, 98 (2020).
- [30] Y. Zhou and A. Rinoshika, Comparison between screen and triangular cylinder far-wakes, *Exp. Therm. Fluid Sci.* **27**, 629 (2003).
- [31] A. Rinoshika and Y. Zhou, Effects of initial Conditions on a Wavelet-decomposed Turbulent Near-wake, *Phys. Rev. E* **71**, 046303 (2005).
- [32] A. Rinoshika and Y. Zhou, Effects of initial conditions on wavelet-decomposed self-preserving turbulent structures, *Int. J. Heat Fluid Flow* **28**, 948 (2007).
- [33] A. Rinoshika, T. Zhou, and Y. Zhou, Orthogonal wavelet-decomposed 3-D vorticity in a turbulent cylinder wake, *JSME Int. J., Ser. B* **49**, 1149 (2006).
- [34] T. Zhou, A. Rinoshika, Z. Hao, Y. Zhou, and L. P. Chua, Wavelet multi-resolution analysis of the three vorticity components in a turbulent far wake, *Phys. Rev. E* **73**, 036307 (2006).
- [35] S. F. M. Razali, T. Zhou, A. Rinoshika, and L. Cheng, Wavelet analysis of the turbulent wake generated by an inclined circular cylinder, *J. Turbul.* **11**, N15 (2010).
- [36] A. Rinoshika, Y. Zheng, and E. Shishido, Wavelet multi-resolution analysis on large-eddy simulation of turbulent flow behind a vehicle external mirror, *Int. J. Wavelets Multiresolution Inf. Process.* **11**, 1360007 (2013).
- [37] A. Rinoshika and K. Watanabe, Orthogonal wavelet decomposition of turbulent structures behind a vehicle external mirror, *Exp. Therm. Fluid Sci.* **34**, 1389 (2010).
- [38] A. Rinoshika and H. Omori, Orthogonal wavelet analysis of turbulent wakes behind various bluff bodies, *Exp. Therm. Fluid Sci.* **35**, 1231 (2011).
- [39] Y. Zheng and A. Rinoshika, Multi-scale vortical structure of three-dimensional dune wake flow, *J. Visualization* **18**, 95 (2015).

- [40] S. Fujimoto and A. Rinoshika, Wavelet multi-resolution analysis on turbulent wakes of asymmetric bluff body, *Int. J. Mech. Sci.* **92**, 121 (2015).
- [41] M. Farge, G. Pellegrino, and K. Schneider, Coherent vortex Extraction in 3D Turbulent Flows Using Orthogonal Wavelets, *Phys. Rev. Lett.* **87**, 054501 (2001).
- [42] G. D. Stefano, A. Nejadmalayeri, and O. V. Vasilyev, Wall-resolved wavelet-based adaptive large-eddy simulation of bluff-body flows with variable thresholding, *J. Fluid Mech.* **788**, 303 (2016).
- [43] L. Eshbal, D. Kovalev, V. Rinsky, D. Greenblatt, and R. van Hout, Tomo-PIV measurements in the wake of a tethered sphere undergoing VIV, *J. Fluids Struct.* **89**, 132 (2019).
- [44] H. Wang, Y. Zhou, C. K. Chan, and K. S. Lam, Effect of initial conditions on interaction between boundary layer and a wall-mounted finite-length-cylinder wake, *Phys. Fluids* **18**, 065106 (2006).
- [45] R. J. Hearst, G. Gomit, and B. Ganapathisubramani, Effect of turbulence on the wake of a wall-mounted cube, *J. Fluid Mech.* **804**, 513 (2016).
- [46] H. Mouri, H. Kubotani, T. Fujitani, H. Niino, and M. Takaoka, Wavelet analysis of velocities in laboratory isotropic turbulence, *J. Fluid Mech.* **389**, 229 (1999).
- [47] A. Rinoshika, Y. Zheng, and F. Yan, Wavelet analysis on particle dynamics in a horizontal air–solid two-phase pipe flow at low air velocity, *Exp. Fluids* **52**, 137 (2012).

Correction: The affiliation indicator for the second author contained an error and has been fixed. Minor changes have been made to the Acknowledgment section.